International Journal of Solids and Structures 50 (2013) 863–875

Contents lists available at SciVerse ScienceDirect

International Journal of Solids and Structures

journal homepage: www.elsevier.com/locate/ijsolstr

Finite Element studies on indentation size effect using a higher order strain gradient theory

Suman Guha [a], Sandeep Sangal [a], Sumit Basu [b,*]

[a] Department of Materials Science and Engineering, Indian Institute of Technology Kanpur, Kanpur 208016, Uttar Pradesh, India
[b] Department of Mechanical Engineering, Indian Institute of Technology Kanpur, Kanpur 208016, Uttar Pradesh, India

ARTICLE INFO

Article history:
Received 12 July 2012
Received in revised form 16 September 2012
Available online 5 December 2012

Keywords:
Micro-indentation
Strain gradient viscoplasticity
Finite Element method

ABSTRACT

In this work, a Finite Element implementation of a higher order strain gradient theory (due to Fleck and Hutchinson, 2001) has been used within the framework of large deformation elasto-viscoplasticity to study the indentation of metals with indenters of various geometries. Of particular interest is the indentation size effect (ISE) commonly observed in experiments where the hardness of a range of materials is found to be significantly higher at small depths of indentation but reduce to a lower, constant value at larger depths. That the ISE can be explained by strain gradient plasticity is well known but this work aims to qualitatively compare a gamut of experimental observations on this effect with predictions from a higher order strain gradient theory. Results indicate that many of the experimental observations are qualitatively borne out by our simulations. However, areas exist where conflicting experimental results make assessment of numerical predictions difficult.

1. Introduction

Indentation is used extensively to measure the hardness of materials, which in turn can be used to predict mechanical properties like modulus and strength. Tabor (1951) and Johnson (1970) have established relationships between the hardness of a material and its mechanical properties when the size of the indents is large and conventional plasticity theory applies.

While indenting a material with indenters of self-similar geometries like cones or pyramids, the measured hardness turns out to be much higher at small depths of indentation—a fact that has been called the indentation size effect (ISE). The ISE has assumed significance with the advent of depth and load sensing indentation techniques which enable researchers to measure hardness from load displacement curves rather than from the residual impression and therefore, enable hardness measurements at extremely small depths of indentation. Given the small volume of material involved, these techniques are especially useful for measuring properties of structures like thin films and multilayers (see for details Freund and Suresh, 2003). However, the correlation between the micro or nano hardness data to the mechanical properties is complicated by the existence of the ISE.

Several explanations for the ISE have been proposed in the literature. Firstly, it has been attributed to experimental artifacts. This is most strikingly demonstrated (see Pharr et al., 2010) by contrasting the data of McElhaney et al. (1998) and Liu and Ngan (2001) for nano-indentation hardness of (111) copper single crystals. While the experiments differed only in surface preparation techniques for the samples, the former study exhibits a pronounced ISE in stark contrast to the latter. A second set of explanations suggest that the ISE is at least partly affected by the surface roughness (e.g., Kim et al., 2007) and wear and rounding of sharp indenter tips during indentation (Qiao et al., 2010).

The ISE has motivated the development of a size dependent plasticity at micron scales. Mechanism based models of size dependent plasticity, pioneered by Nix and Gao (1998) are based on the concept of geometrically necessary dislocations (GND) which have to be present near the indentation in order to accommodate the volume of the material displaced by the indenter. The GNDs exist in addition to statistically stored dislocations (SSD) produced by uniform straining and the total dislocation density ρ_t is related to the flow stress σ_0 by the Taylor relation as

$$\sigma_0 = \sqrt{3}\alpha G b \sqrt{\rho_t}, \tag{1}$$

where, α is the Taylor factor, G the shear modulus and b the Burger's vector. Combined with the Tabor relation that the hardness $H = 3\sigma_0$, simple geometric arguments lead to an estimate of the density of GNDs as

$$\rho_G = \frac{3\tan^2\theta}{2bh}, \tag{2}$$

where θ is the angle defining the self similar indentation by a rigid cone. Further, the above equation shows that the GND density is

* Corresponding author. Tel.: +91 512 259 7506; fax: +91 512 259 7408.
E-mail address: sbasu@iitk.ac.in (S. Basu).

0020-7683/$ - see front matter © 2012 Elsevier Ltd. All rights reserved.
http://dx.doi.org/10.1016/j.ijsolstr.2012.10.017

inversely proportional to the depth of indentation h, a fact that directly provides an explanation for the ISE. Key assumptions that lead to this conclusion are (i) the total dislocation density is the sum of the GNDs and SSDs, i.e. $\rho_t = \rho_G + \rho_S$ and (ii) the GNDs are confined to a hemispherical volume with radius equal to the radius of contact a. The above considerations then lead to

$$\frac{H}{H_0} = \sqrt{1 + \frac{h^*}{h}}, \tag{3}$$

where H_0 represents the macroscopic hardness that is approached asymptotically at large depths and h^* is a length scale defining the depth below which the ISE becomes significant. The above equation establishes an experimentally verifiable linear relationship between $(H/H_0)^2$ and $1/h$.

For a number of materials, at relatively large indent sizes, the Nix and Gao (1998) model seems to work reasonably well. For (111) copper (McElhaney et al., 1998) and (110) silver (Ma and Clarke, 1995) single crystals indented with a Berkovich indenter, H^2 varies linearly as $1/h$ till a depth of about $h = 0.2$ μm. Similarly, Poole et al. (1996) showed that for annealed and work hardened polycrystalline copper, the data for H^2 was linear within depths of 10 to 0.6 μm, though, as pointed out by Begley and Hutchinson (1998), less convincingly than in the case of single crystal copper and silver. Moreover, data from Lim and Chaudhri (1999) for annealed copper shows large deviation from linearity at depths less than 1 μm (they also show non-monotonic behavior with depth for work hardened copper). Hardness data for iridium (Swadener et al., 2002) and MgO (Feng and Nix, 2004) exhibit very limited regions of linearity. In fact, Elmustafa and Stone (2003), from an analysis of indentation data for polycrystalline copper, aluminium, silver and brass, suggest that H^2 follows a bilinear relationship with $1/h$, with a higher slope in the micro-hardness regime.

Several important, albeit empirical, modifications to the basic idea proposed by Nix and Gao (1998) have also been suggested. For example, Durst et al. (2005) introduced a correction factor accounting for the fact that the hemispherical volume storing the GNDs beneath the indenter has a radius significantly larger than the contact radius. Shi et al. (2004) have introduced a Nye factor to account for crystallographic constraints on SSD and GND densities. Huang et al. (2006) placed a limit on the maximum GND density that can develop below the indenter and using this limit as an additional adjustable parameter, could fit the data for iridium and MgO to a reasonable extent.

An important alternative formulation for plasticity at small scales is provided by the strain gradient plasticity model proposed by Fleck and Hutchinson (1997) and subsequently reformulated (Fleck and Hutchinson, 2001) to a framework that is more suitable for numerical applications and closer in spirit to the early models of Aifantis (1984). The mathematical structure of strain gradient based models is different from the Nix and Gao (1998) model in the sense that more boundary conditions compared to conventional theories of plasticity need to be specified. As a result, the theory can capture boundary layer phenomenon related to surfaces and interfaces. These theories aspire to provide a framework for explaining size effects not only in indentation but also for several other problems where a size effect manifests e.g. bending of thin beams (Stölken and Evans, 1998) and torsion of fine wires (Fleck et al., 1994).

It is clear from the Finite Element (FE) analyses of Huang et al. (2006) and those of Begley and Hutchinson (1998) and Wei and Hutchinson (2003), that both the small scale plasticity theories can capture the ISE. However, though Wei and Hutchinson (2003) could fit the nano-hardness data for iridium through their simulations, a comprehensive study of the capabilities of these models to capture key experimental features of nano and micro-indentation experiments for a range of polycrystalline materials seems to be lacking.

In this work, we use a large deformation based Finite Element (FE) implementation of the viscoplastic version (Borg et al., 2006) of the reformulated Fleck and Hutchinson (2001) model to assess its applicability to problems of indentation. To this end, we solve a number of 2 dimensional indentation geometries for a range of representative materials with a view to gain insights into the origins of ISE.Qualitative connections with experimental results are made wherever necessary. The present numerical framework is well suited for reproducing the experimental hardness versus depth behavior of a wide class of metals and thereby capture the ISE quantitatively. However, several experimental artifacts contribute to the ISE alongwith the generation of GNDs due to indentation. At this stage it is not possible to separate these contributions and we limit our attention to understanding whether the strain gradient plasticity model yields predictions that are in line with experimental and other lower level non-continuum simulations.

2. Material model

2.1. Basic kinematics

The displacement of a point in space is denoted as,

$$u_i = x_i - X_i, \tag{4}$$

where X_i is a material point and x_i is the position of the same in the deformed configuration. The deformation gradient tensor and the velocity gradient tensor are given in the conventional manner as

$$F_{ij} = \frac{\partial x_i}{\partial X_j} \text{ and} \tag{5}$$

$$L_{ij} = \frac{\partial \dot{u}_i}{\partial x_j} = \dot{u}_{i,j}. \tag{6}$$

The strain rate is derived from the symmetric part of L_{ij} as

$$\dot{\epsilon}_{ij} = \frac{1}{2}(L_{ij} + L_{ji}). \tag{7}$$

Further $\dot{\epsilon}_{ij}$ is decomposed additively into the elastic and the plastic part as

$$\dot{\epsilon}_{ij} = \dot{\epsilon}^e_{ij} + \dot{\epsilon}^p_{ij}. \tag{8}$$

The skew-symmetric part of the velocity gradient tensor is

$$\dot{\omega}_{ij} = \frac{1}{2}(L_{ij} - L_{ji}). \tag{9}$$

It is also assumed that the material follows von-Mises material behavior and the normality rule holds true under the present formulation, which implies,

$$\dot{\epsilon}^p_{ij} = \frac{3\sigma'_{ij}}{2\sigma_e}\dot{\epsilon}^p = m_{ij}\dot{\epsilon}^p, \tag{10}$$

where $\dot{\epsilon}^p$ is the equivalent plastic strain defined as $\sqrt{2\dot{\epsilon}^p_{ij}\dot{\epsilon}^p_{ij}/3}$ and σ'_{ij} is the deviatoric part of the stress tensor. The tensor $m_{ij} = 3\sigma'_{ij}/2\sigma_e$ is defined in terms of the equivalent stress $\sigma_e = \sqrt{3\sigma'_{ij}\sigma'_{ij}/2}$. In order to incorporate non-local effects due to strain gradient following Fleck and Hutchinson (2001), an effective plastic strain rate is defined in terms of the plastic strain rate and the gradient of plastic strain rate as

$$\dot{E}^{p^2} = \dot{\epsilon}^{p^2} + l_*^2\dot{\epsilon}^p_{,i}\dot{\epsilon}^p_{,i}, \tag{11}$$

where l_* is the characteristic length scale of the material introduced to maintain dimensional consistency.

2.2. Virtual work relation and material model

Under the framework of gradient plasticity the conventional virtual work relation is augmented by the virtual work corresponding to the gradient of plastic strain and its work conjugate, a higher order stress quantity. According to Niordson and Redanz (2004) the virtual work relationship for a gradient plastic material is given as

$$\int_V (\sigma_{ij}\delta\dot{\epsilon}^e_{ij} + Q\delta\dot{\epsilon}^p + \tau_i\delta\dot{\epsilon}^p_{,i})dV = \int_S (T_i\delta\dot{u}_i + t\delta\dot{\epsilon}^p)dS, \tag{12}$$

where left hand side of (12) corresponds to the internal virtual work and the right hand side, the external virtual work. Here, $\sigma_{ij}\delta\epsilon^e_{ij}$ represents the virtual work due the elastic strain increment and Q is a scalar microstress which contributes to the virtual work due to the plastic strain increment. Additionally, τ_i is the higher order stress, work conjugate to the virtual incremental quantity $\delta\epsilon^p_{,i}$ (the gradient of plastic strain). The above virtual work relation is different from the corresponding conventional equation in a sense that both the displacement and the equivalent plastic strain are considered to be independent kinematic quantities. As a consequence of the above consideration additional boundary conditions on $\dot{\epsilon}^p$ or on the higher order tractions need to be imposed. The right hand side of (12) hence represents the external virtual work by the conventional tractions and the external virtual work due to higher-order tractions. The equilibrium equations and the boundary conditions can be obtained from (12) by the application of the Gauss' theorem and noting that (12) holds true for any arbitrary variations of $\dot{u}_i$ and $\dot{\epsilon}^p$. The equilibrium equations consist of the conventional equilibrium equation $\sigma_{ji,j} = 0$, with an additional consistency condition given by,

$$Q = \sigma_e + \tau_{i,i}. \tag{13}$$

The boundary conditions are,

$$T_i = \sigma_{ji}n_j, \text{ and} \tag{14}$$

$$t = \tau_i n_i, \tag{15}$$

where n_i is the unit normal to the surface where the boundary tractions T_i or the higher order tractions t are specified. Additionally boundary conditions of the form,

$$u_i = u^*_i \text{ and} \tag{16}$$

$$\epsilon^p = \epsilon^{p*}, \tag{17}$$

on some parts of the boundary may be prescribed. Here, u^*_i and ϵ^{p*} are imposed displacement or equivalent plastic strain.

2.3. Updated Lagrangian framework

With a view to develop a finite deformation model under updated Lagrangian framework, the virtual work relation in (12) is now rewritten in the reference configuration following Niordson and Redanz (2004). The Kirchhoff stress measures for various stress quantities are defined as,

$$\zeta_{ij} = J\sigma_{ij}, \tag{18}$$

$$\sigma^\zeta_e = J\sigma_e, \tag{19}$$

$$q = JQ, \text{ and} \tag{20}$$

$$\rho_i = J\tau_i. \tag{21}$$

Similarly, the first Piola–Kirchhoff stress measures are defined as,

$$s_{ij} = JF^{-1}_{ik}\sigma_{kj} = F^{-1}_{ik}\zeta_{kj}, \text{ and} \tag{22}$$

$$\varrho_i = JF^{-1}_{ik}\tau_k = F^{-1}_{ik}\rho_k, \tag{23}$$

where J is the determinant of the deformation gradient tensor. Using the above relations in (12), the virtual work equation in the reference configuration is obtained as follows,

$$\int_{V_0} (s_{ij}\delta\dot{F}_{ij} + (q - \sigma^\zeta_e)\delta\dot{\epsilon}^p + \varrho_i\delta\dot{\epsilon}^p_{,0i})dV_0 = \int_{S_0} (T_{0i}\delta\dot{u}_i + t_0\delta\dot{\epsilon}^p)dS_0. \tag{24}$$

The incremental version of the above virtual work equation in the reference configuration becomes:

$$\int_{V_0} (\dot{s}_{ij}\delta\dot{F}_{ij} + (\dot{q} - \dot{\sigma}^\zeta_e)\delta\dot{\epsilon}^p + \dot{\varrho}_i\delta\dot{\epsilon}^p_{,0i})dV_0 = \int_{S_0} (\dot{T}_{0i}\delta\dot{u}_i + \dot{t}_0\delta\dot{\epsilon}^p)dS_0. \tag{25}$$

As the constitutive relations will be formulated in terms of the Jaumann rate of Kirchhoff stress $\left(\overset{\triangledown}{\underset{ij}{\zeta}}\right)$ and convected rate of the higher order Kirchhoff stress $\left(\overset{\vee}{\underset{i}{\rho}}\right)$, (Borg et al., 2006) the following identities have been used under updated Lagrangian framework,

$$\dot{s}_{ij} = \overset{\triangledown}{\underset{ij}{\zeta}} - \sigma_{kj}\dot{\epsilon}_{ik} - \sigma_{ik}\dot{\epsilon}_{jk} + \sigma_{ik}L_{jk}, \text{ and} \tag{26}$$

$$\dot{\varrho}_i = \overset{\vee}{\underset{i}{\rho}}. \tag{27}$$

As mentioned in Niordson and Redanz (2004), the convected rate for higher order stress vector is employed in stead of the Jaumann rate because using the latter to define the constitutive relation for higher order stress yields a non-symmetric stiffness matrix. Finally the virtual work relation in the reference configuration takes the following form:

$$\int_V (\overset{\triangledown}{\zeta_{ij}}\delta\dot{\epsilon}_{ij} - \sigma_{ij}(2\dot{\epsilon}_{ik}\delta\dot{\epsilon}_{kj} - L_{kj}\delta L_{ki}) + (\dot{q} - \dot{\sigma}^\zeta_e)\delta\dot{\epsilon}^p + \overset{\vee}{\underset{i}{\rho}}\delta\dot{\epsilon}^p_{,0i})dV = \int_S (\dot{T}_{0i}\delta\dot{u}_i + \dot{t}_0\delta\dot{\epsilon}^p)dS - \frac{1}{\Delta t}[\text{Eqm Corr}], \tag{28}$$

where [Eqm Corr] is given by,

$$\text{Eqm Corr} = \int_V (\sigma_{ij}\delta\dot{\epsilon}_{ij} + (Q - \sigma_e)\delta\dot{\epsilon}^p + \tau_i\delta\dot{\epsilon}^p_{,0i})dV - \int_S (T_{0i}\delta\dot{u}_i + t_0\delta\dot{\epsilon}^p)dS, \tag{29}$$

and is required in order to prevent the solution from drifting with time from equilibrium for large strain problems.

2.4. Constitutive relations

In this section the constitutive relations are defined by following a viscoplastic material model as described in Borg et al. (2006). A viscoplastic potential Φ is defined which is a function of a generalized effective stress σ_c, which is work conjugate to the effective plastic strain rate $\dot{E}^p$. It is assumed that the higher order stress quantities are derivable from the viscoplastic potential in the following manner,

$$\begin{aligned} \sigma_c &= \frac{\partial\Phi}{\partial\dot{E}^p}, \\ q &= \frac{\partial\Phi}{\partial\dot{\epsilon}^p} = \sigma_c\frac{\partial\dot{E}^p}{\partial\dot{\epsilon}^p}, \text{ and} \\ \rho_i &= \frac{\partial\Phi}{\partial\dot{\epsilon}^p_{,i}} = \sigma_c\frac{\partial\dot{E}^p}{\partial\dot{\epsilon}^p_{,i}}. \end{aligned} \tag{30}$$

Using (11) and (30), the constitutive relations for a strain gradient viscoplastic material becomes,

$$q = \frac{\sigma_c}{\dot{E}^p}\dot{\epsilon}^p, \tag{31}$$

$$\rho_i = \frac{\sigma_c}{\dot{E}^p} l_*^2 \dot{\epsilon}^p_{,i}, \text{ and} \tag{32}$$

$$\sigma_c^2 = q^2 + l_*^{-2}\rho_i\rho_i. \tag{33}$$

In case $l_* = 0$ (i.e. for a conventional material) σ_c reduces to q. The viscoplastic material behavior is modeled as,

$$\sigma_c = \sigma_0\left(1 + \frac{E^p}{\epsilon_0}\right)^{1/n}\left(\frac{\dot{E}^p}{\dot{\epsilon}_0}\right)^m, \tag{34}$$

where σ_0 is the initial yield strength of the material and $g(E^p) = \sigma_0(1 + E^p/\epsilon_0)^{1/n}$ describes the uniaxial strain hardening response of the material. The quantity n is the strain hardening exponent, m governs the strain rate sensitivity and $\dot{\epsilon}_0$ is the reference strain rate. When $\dot{E}^p$ is close to or less than $\dot{\epsilon}_0$, Eq. (34) exhibits rate-independent behavior as $\sigma_c \approx g(E^p)$. The strain at initial yield is $\epsilon_0 = \sigma_0/E$. It is to be noticed that the above material behavior incorporates E^p and $\dot{E}^p$ in the power law, instead of ϵ^p and $\dot{\epsilon}^p$.

The incremental constitutive relations for the above viscoplastic material model can be summarized as,

$$\overset{\triangledown}{\underset{ij}{\zeta}}\Delta t = R_{ijkl}(\Delta\epsilon_{kl} - m_{kl}\Delta\epsilon^p), \tag{35}$$

$$\dot{q}\Delta t = \frac{\sigma_c}{\dot{E}^p}\left((m-1)\frac{\dot{\epsilon}^p}{\dot{E}^p}\Delta\dot{E}^p + \Delta\dot{\epsilon}^p\right) + \left(\frac{\dot{E}^p}{\dot{\epsilon}_0}\right)^m \frac{dg}{dE^p}\dot{\epsilon}^p\Delta t, \text{and} \tag{36}$$

$$\overset{\vee}{\rho}_i\Delta t = l_*^2\left(\frac{\sigma_c}{\dot{E}^p}\left((m-1)\frac{\dot{\epsilon}^p_{,i}}{\dot{E}^p}\Delta\dot{E}^p + \Delta\dot{\epsilon}^p_{,i}\right) + \left(\frac{\dot{E}^p}{\dot{\epsilon}_0}\right)^m \frac{dg}{dE^p}\dot{\epsilon}^p_{,i}\Delta t\right). \tag{37}$$

The elasticity tensor R_{ijkl} is given by,

$$R_{ijkl} = \frac{E}{1+\nu}\left(\frac{1}{2}(\delta_{ik}\delta_{jl} + \delta_{il}\delta_{jk}) + \frac{\nu}{1-2\nu}\delta_{ij}\delta_{kl}\right), \tag{38}$$

and increment in the effective plastic strain rate using (11) is given by,

$$\Delta\dot{E}^p = \frac{\dot{\epsilon}^p}{\dot{E}^p}\Delta\dot{\epsilon}^p + \frac{l_*^2\dot{\epsilon}^p_{,i}}{\dot{E}^p}\Delta\dot{\epsilon}^p_{,i}. \tag{39}$$

2.5. Finite Element formulation

For FE analyses, we use isoparametric quadratic triangular elements. In addition to the increment of displacement components Δu_i, increment of equivalent plastic strain rate $\Delta\dot{\epsilon}^p$ is also used as a degree of freedom for each node. Both the displacement increments and the increments of equivalent plastic strain rate are interpolated within the element using quadratic functions in terms of their respective nodal components ΔD_N and $\Delta\dot{\epsilon}^p_N$ as,

$$\Delta u_i = \sum_{N=1}^{2k} N_i^N \Delta D_N, \text{and} \tag{40}$$

$$\Delta\dot{\epsilon}^p = \sum_{N=1}^{k} M^N \Delta\dot{\epsilon}^p_N, \tag{41}$$

where N_i and M are the shape functions and $k = 6$ is the number of nodes used for interpolation. Accordingly from the above relations, increments in the velocity gradient and the strain tensor can be represented in terms of the nodal displacement increment as,

$$\Delta L_{ij} = \sum_{N=1}^{2k} N^N_{i,j}\Delta D_N, \text{ and} \tag{42}$$

$$\Delta\epsilon_{ij} = \sum_{N=1}^{k} E_{ij}^N \Delta D_N, \quad \text{where, } E_{ij} = \frac{1}{2}(N^N_{i,j} + N^N_{j,i}). \tag{43}$$

In a similar manner, the gradient of equivalent plastic strain rate is given by,

$$\Delta\dot{\epsilon}^p_{,i} = \sum_{N=1}^{k} M^N_{,i}\Delta\dot{\epsilon}^p_N. \tag{44}$$

Finally the virtual work relation is discretized using the above relations and can be expressed in the following form:

$$\begin{bmatrix} \boldsymbol{K}_e & \boldsymbol{0} \\ \boldsymbol{K}_{ep} & \boldsymbol{K}_p \end{bmatrix}\begin{bmatrix} \Delta\boldsymbol{D}_N \\ \Delta\dot{\epsilon}^p_N \end{bmatrix} = \begin{bmatrix} \Delta\boldsymbol{F}_1 \\ \Delta\boldsymbol{F}_2 \end{bmatrix} + \begin{bmatrix} \boldsymbol{C}_1 \\ \boldsymbol{C}_2 \end{bmatrix}, \tag{45}$$

where the elastic stiffness matrix

$$\boldsymbol{K}_e^{NM} = \int_V (E_{ij}^N R_{ijkl} E_{kl}^M + \sigma_{ij}(N^M_{k,j}N^N_{k,i} - 2E^M_{ik}E^N_{jk}))dV, \tag{46}$$

the coupling matrix

$$\boldsymbol{K}_{ep}^{NM} = -\int_V m_{ij}R_{ijkl}E^M_{kl}M^N dV \tag{47}$$

and the plastic stiffness matrix

$$\begin{aligned}\boldsymbol{K}_p^{NM} = \int_V \Bigg(&\left(\frac{\dot{\epsilon}^p}{\dot{E}^{p^2}}(m-1)q + \frac{\sigma_c}{\dot{E}^p}\right)M^M M^N + \frac{l_*^2\dot{\epsilon}^p_{,i}}{\dot{E}^{p^2}}(m-1)qM^M M^N_{,i} \\ &+ \frac{\dot{\epsilon}^p}{\dot{E}^{p^2}}(m-1)\rho_i M^M_{,i}M^N + \frac{l_*^2\dot{\epsilon}^p_{,i}}{\dot{E}^{p^2}}(m-1)\rho_k M^M_{,k}M^N_{,i} + \frac{l_*^2\sigma_c}{\dot{E}^p}M^M_{,i}M^N_{,i}\Bigg)dV,\end{aligned} \tag{48}$$

need to be calculated for each element. The force vectors on the right of Eq. (45) are given by

$$\Delta\boldsymbol{F}_1^N = \int_S \Delta T_i N_i^N dS + \Delta t\int_V E_{ij}^N R_{ijkl}m_{kl}\dot{\epsilon}^p dV, \tag{49}$$

where the conventional force vector is augmented by a volume force contribution from (35). The force vector corresponding to the higher order traction is given by,

$$\begin{aligned}\Delta\boldsymbol{F}_2^N = \int_S \Delta\rho_i n_i M^N dS - \Delta t\int_V \Bigg(&\left(m_{ij}R_{ijkl}m_{kl}\dot{\epsilon}^p + \dot{\epsilon}^p\frac{dg}{dE^p}\left(\frac{\dot{E}^p}{\dot{\epsilon}_0}\right)^m\right)M^N \\ &+ l_*^2\dot{\epsilon}^p_{,i}\frac{dg}{dE^p}\left(\frac{\dot{E}^p}{\dot{\epsilon}_0}\right)^m M^N_{,i}\Bigg)dV.\end{aligned} \tag{50}$$

Further the force vectors corresponding to the equilibrium correction terms are

$$\boldsymbol{C}_1^N = -\int_V \sigma_{ij}E^N_{ij}dV + \int_S T_i N_i^N dS, \text{and} \tag{51}$$

$$\boldsymbol{C}_2^N = -\int_V ((Q - \sigma_e)M^N + \tau_i M^N_i)dV + \int_S tM^N dS. \tag{52}$$

It can be observed that the system of equations in (45) are decoupled, in the sense that once ΔD_N is solved, $\Delta\dot{\epsilon}^p_N$ can be obtained using ΔD_N.

Six noded triangular elements with three Gauss integration points have been used in all the simulations reported here. Though stress oscillations ave been reported for these elements by Borst and Pamin (1996), we note that the present structure of the FE equations in Eq. (45) is significantly different from those dealt with by Borst and Pamin (1996) or Niordson and Redanz (2004). We obtained consistent results with these elements and no stress locking was noted. However, as observed by Mikkelsen and Goutianos (2009), the use of $\boldsymbol{C}_2^N$ in simulations lead to numerical problems and therefore, $\boldsymbol{C}_2^N = 0$ has been assumed.

After the displacement increments and the plastic strain rate increments are solved, the various stress rates can be updated using the constitutive relations in (36, 37). The increments of Cauchy stress tensor and the higher order stress vector are calculated from the Jaumann rate of Kirchhoff stress tensor and the convective rate of higher order stress vector respectively according to,

$$\Delta\sigma_{ij} = \overset{\triangledown}{\underset{ij}{\zeta}}\Delta t + \Delta\omega_{ik}\sigma_{kj} + \sigma_{ik}\omega_{jk} - \sigma_{ij}\Delta\epsilon_{kk}, \text{ and} \tag{53}$$

$$\Delta\tau_i = \overset{\vee}{\underset{i}{\rho}}\Delta t + \Delta L_{ik}\tau_k - \tau_i\Delta\epsilon_{kk}. \tag{54}$$

Further effective stress, σ_c is obtained from (33) and thereafter the equivalent plastic strain rate, $\dot{\epsilon}^p$ and its gradient, $\dot{\epsilon}^p_{,i}$ is obtained from (31) and (32).

3. Results and discussions

3.1. Johnson's model for indentation incorporating strain gradient plasticity

Strain gradient plasticity models are expected to exhibit an ISE. This can easily be seen from a simple void model similar to that proposed by Johnson (1970) for conventional plasticity. The idea for wedge indentation is shown in Fig. 1. A small volume of material of radius a, equal to the half width of the contact is assumed to be under pure hydrostatic stress $-p_0\delta_{ij}$. This implies that the solution to stresses, strains and displacements for $r \geqslant a$ are similar to that for a cylindrical void in an infinite block internally pressurized to p_0 at $r = a$ or equivalently, to a traction free void of the same radius subjected to remote stresses $\sigma^\infty_{ij} = p_0\delta_{ij}$.

The velocity field for this problem, within the framework of small deformation theory, is given at r as

$$\dot{u}_r = \frac{\dot{V}}{2\pi r} \text{ and}$$

$$\dot{u}_\theta = \dot{u}_z = 0,$$

where $\dot{V}$ gives the rate of volume expansion of the void. The above velocity field leads to a strain rate field given as

$$\dot{\epsilon}_{rr} = \frac{\partial\dot{u}_r}{\partial r} = -\frac{\dot{V}}{2\pi r^2},$$

$$\dot{\epsilon}_{\theta\theta} = \frac{1}{r}\frac{\partial\dot{u}_\theta}{\partial\theta} + \frac{\dot{u}_r}{r} = \frac{\dot{V}}{2\pi r^2} = -\dot{\epsilon}_{rr} \text{ and,}$$

$$\dot{\epsilon}_{zz} = 0.$$

Following Fleck and Hutchinson (2001), the boundary value problem described above can be stated as that of minimizing the functional

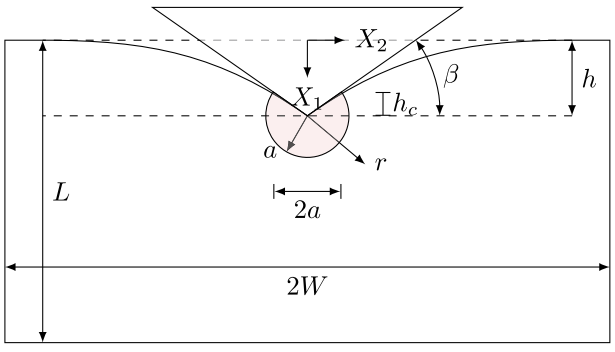

Fig. 1. Schematic of the wedge indentation model.

$$I(\dot{\epsilon}_p, \dot{\epsilon}_{p,r}, r) = \frac{1}{2}\int_a^\infty \left\{4\mu\left(-\frac{\dot{V}}{2\pi r^2} + \frac{\sqrt{3}}{2}\dot{\epsilon}_p\right)^2 + h(E_p)\dot{E}_p^2\right\}2\pi r dr, \tag{55}$$

the minimization of which leads to the ordinary differential equation,

$$\frac{d^2\dot{\epsilon}_p}{d\hat{r}^2} = -\frac{1}{\hat{r}}\frac{d\dot{\epsilon}_p}{d\hat{r}} + \left(\frac{a}{l_*}\right)^2\left(1 + \frac{3\mu}{h(E_p)}\right)\dot{\epsilon}_p - \frac{\sqrt{3}\mu}{h(E_p)}\frac{\dot{V}}{V}\left(\frac{a}{l_*}\right)^2\frac{1}{\hat{r}^2}. \tag{56}$$

In the above, we have used $\hat{r} = r/a$. The above equation has to be solved numerically with the boundary condition $\dot{\epsilon}_p(\hat{r}_\infty) = 0$ and $d\dot{\epsilon}_p/d\hat{r}(1) = 0$. The latter condition specifies that the surface of the void is free of higher order tractions. Further, $h(E^p) = (E/n)(E^p/\epsilon_0)^{(1-n)/n}$. Once $\dot{\epsilon}_p(\hat{r})$ is obtained, the remote stress can be obtained using

$$\frac{1}{2}\dot{\sigma}_\infty\dot{V} = I. \tag{57}$$

The variation of σ_∞/σ_0 with $\Delta V/\epsilon_0 V$ is shown in Fig. 2(a) for different values of l_*/a at a constant $\dot{V}$. To connect with the indentation problem, at a depth of indentation h, we identify V with twice the size of the region of constant pressure below the indenter and ΔV with twice the volume displaced by it (Wei and Hutchinson, 2003). As a result, a self similar indenter geometry like the wedge has

$$\frac{\Delta V}{\epsilon_0 V} = \frac{2\tan\beta}{\epsilon_0\pi}. \tag{58}$$

Note that the measure of strain is independent of the indentation depth. For our geometry and material properties ($\beta = 15^o$, $\epsilon_0 = 0.001$), $\Delta V/\epsilon_0 V = 170$. When we plot σ_∞/σ_0 against a/l_* at $\Delta V/\epsilon_0 V = 170$, as in Fig. 2(b), a clear size effect is seen (note that σ_∞ has to be identified with the hardness H in this model). However, as shown in Fig. 2(c), when $(\sigma_\infty/\sigma_0)^2$ is plotted against l_*/a, a linear variation is not obtained. This is due to the fact that the current model connects the total dislocation density as in Eq. (11) and does not assume it to be a sum of the SSD and GND densities. Under the assumption inherent in Eq. (11), the square of the hardness should vary as $\sqrt{1 + (h^*/h)^2}$, which is depicted in Fig. 2(c).

The void model demonstrates an intuitively obvious fact: that a model of plasticity that incorporates a length scale is expected to exhibit an ISE. A more detailed simulation is needed to figure out if all experimentally observed features of the ISE are indeed captured by such models of plasticity.

3.2. Finite Element studies of wedge indentation

In this work, simulations of indentation are performed using different indenter geometries on a substrate whose size is $L \times 2W$ with both L and W much larger than l_* (see Fig. 1). The surface at $X_1 = L$ is assumed to have $\dot{u}_1 = \dot{\epsilon}_p = 0$, while those at $X_2 = \pm W$ are traction free. For all practical purposes, since L and W are always taken to be larger than $250l_*$ (unless otherwise mentioned), the subsequent results are insensitive to these boundary conditions. We have performed a mesh sensitivity analysis for the wedge indentation problem and have used a mesh with sufficient refinement, especially close to the tip of the indenter. A circular region of radius $2l_*$ centered at the indenter tip has been refined such that the smallest element has sides of $0.03l_*$. A total of 646 six noded triangular elements have been used in the largest domains.

The hardness H is calculated based on the actual length of contact $2a$, as shown in Fig. 1. In general, $2a$ differs from the nominal length of contact derived from the depth of indentation h ($A_N = 2h/\tan\beta$) due to sink in or pile up. Moreover, if S is the

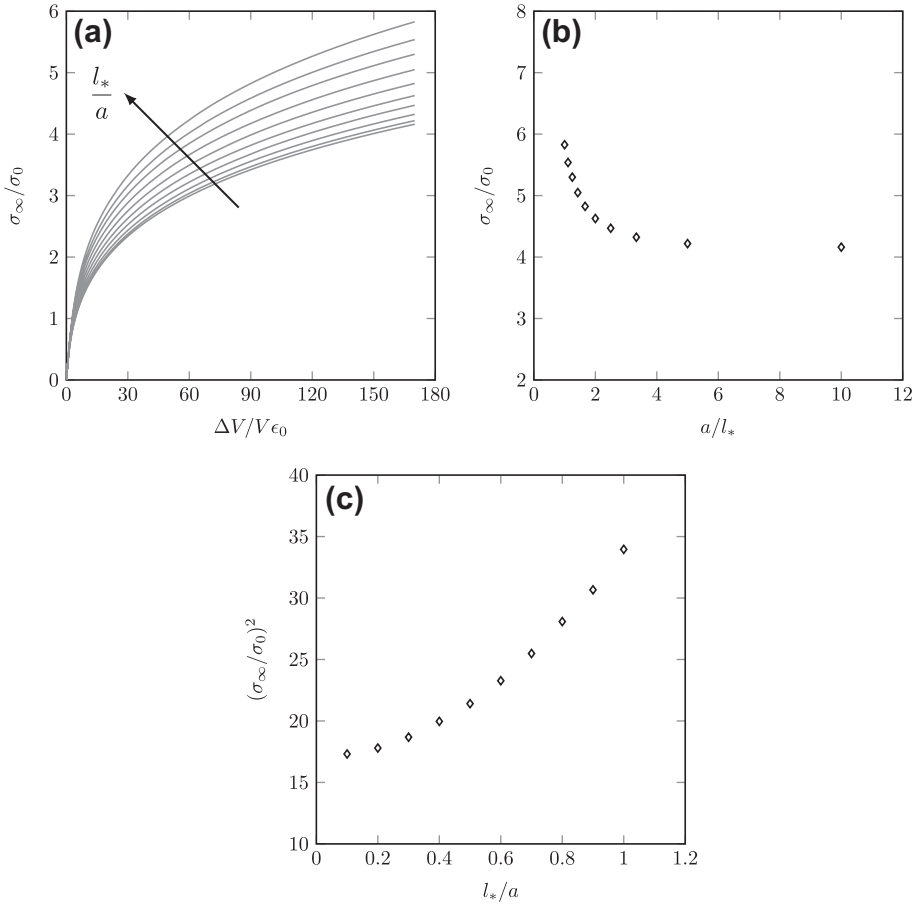

Fig. 2. (a) Variation of σ_∞/σ_0 with $\Delta V/V\epsilon_0$ for varying l_*/a values, (b) variation of σ_∞/σ_0 with a/l_* and (c) variation of the square of σ_∞/σ_0 with l_*/a for $\Delta V/V\epsilon_0 = 170$.

portion of the deformed surface $X_1 = 0$ that is in contact with the indenter, we have

$$\dot{u}_1 = -\dot{h}, \quad u_2 = 0 \quad \text{on } S. \tag{59}$$

The rate of loading $\dot{h}$ is maintained very low at $0.005 l_*$ s^{-1}. The total load due to the indenter on the substrate is given as

$$P = -\int_{-W}^{W} T_1(x_2, h)dx_2, \tag{60}$$

with $T_i = \sigma_{ij}n_j$ being the traction on a surface in terms of the Cauchy stress σ_{ij} and outward normal component n_i. Finally, the hardness is defined as the force per unit actual contact length and

$$H = \frac{P}{2a}. \tag{61}$$

3.2.1. Basic features of micro-indentation

Several simulation studies of indentation problems with conventional plasticity have been reported in the literature (Bhattacharya and Nix, 1988b; Bhattacharya and Nix, 1988a; Bhattacharya and Nix, 1991). Studies of indentation with strain gradient plasticity has been reported by Begley and Hutchinson (1998), Wei and Hutchinson (2003) and Huang et al. (2006). Salient differences in plastic strain and mean stress fields that arise between conventional and strain gradient based analyses are discussed here.

Three different materials have been considered. Materials #1 and #2 are low yielding ones with $\epsilon_0 = 0.001$ but $n = 0.2$ and 0.5 respectively. Though we do not intend to model specific materials, the former is representative of a material like aluminium while the latter represents annealed copper or iridium. Material #3 is a material with $\epsilon_0 = 0.01$ and $n = 0.2$ representing work hardened copper or MgO. In all simulations reported herein, the reference strain rate is $\dot{\epsilon}_0 = 0.005$ s^{-1} and $m = 0.04$, which effectively simulates a rate independent situation.

Fig. 3(a) and (b) show respectively, the variation in the load P/σ_0 and hardness H/H_0 variations with depth of indentation h/l_*. Here, H_0 is the hardness from an analysis with conventional plasticity where no depth dependence is observed. The difference in the load-depth plots between the conventional and strain gradient cases occur at small values of depth. As shown in Fig. 3(a), the strain gradient case needs a significantly higher load for indenting the sample to the same depth. Also, as shown in the inset, during unloading from small depths, the initial unloading slope of the case with strain gradients is much higher than the conventional one. At large depths however, the load required to indent to a certain h, as well as the initial slope of the unloading curve is almost equal. In fact, for $h/l_* > 5$, there is very little difference in the load-depth curves for the two cases. The larger initial slope of the unloading curve at small values of h implies that the residual area left by the indenter will be smaller in strain gradient plasticity. When methods like those by Oliver and Pharr (2004) are used to calculate hardness, a much higher value than what is expected from conventional plasticity will result.

A typical variation of H/H_0 for the case with $\epsilon_0 = 0.001$ and $n = 0.2$ has been shown in Fig. 3(b). The expected ISE is observed in these plots where the hardness increases sharply at small depths of indentation. As evident from Eq. (11), the square of the total dislocation density in the current model is the sum of the squares of the densities of geometrically and statistically stored dislocations. This is in contrast to Eq. (3), which assumes a linear combination of SSDs and GNDs. Thus, poor fits are produced when Eq. (3) are used. However, in Fig. 3(b), we show a fit assuming that

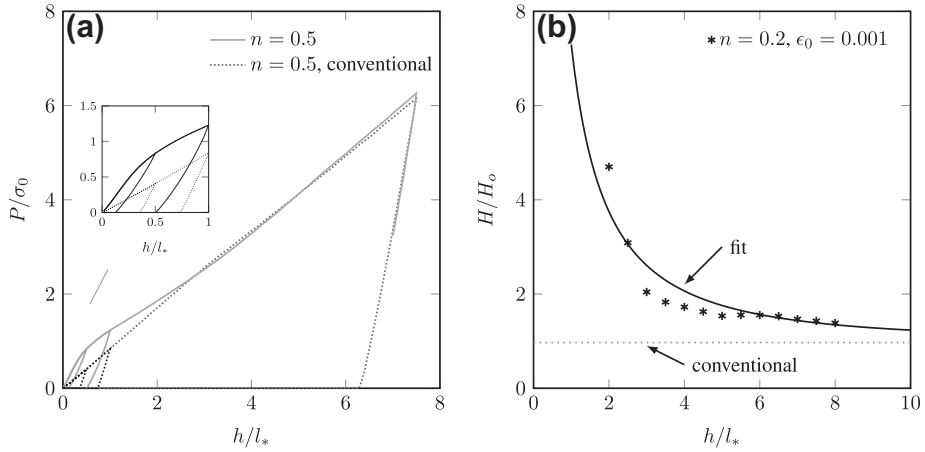

Fig. 3. Variation of (a) the load P/σ_0 and (b) hardness H/H_0 with the depth of indentation h/l_* for $n = 0.2$ and $\epsilon_0 = 0.001$. In (b), the solid curve indicates fits using Eq. (62).

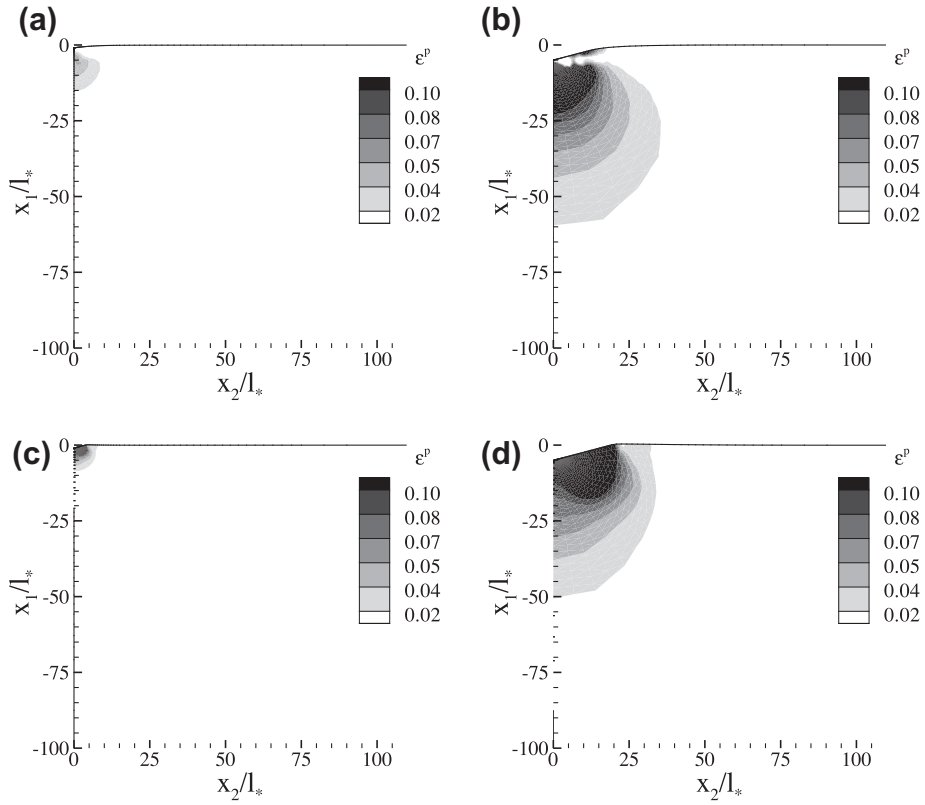

Fig. 4. Contour plots of equivalent plastic strain ϵ^p under the indenter at depths $h/l_* = 1$ ((a) and (c)) and 5 ((b) and (d)), for a low yielding material with $\epsilon_0 = 0.001$ and $n = 0.2$. The figures on the top row are for strain gradient plasticity, while those on the bottom are for conventional plasticity.

$$\frac{H}{H_0} = \sqrt{\left\{1 + \left(\frac{h^*/l_*}{h/l_*}\right)^2\right\}}, \tag{62}$$

which is commensurate with the assumption inherent in Eq. (11). The fit is obtained with $h^*/l_* \simeq 8$.

Fig. 4 shows, for wedge indentation, contours of equivalent plastic strain ϵ^p for a representative case with $n = 0.2$ and $\epsilon_0 = 0.001$, at indentation depths of $h/l_* = 1$ and 5. While Fig. 4(c) and (d) pertain to conventional plasticity, Fig. 4(a) and (b) are for strain gradient plasticity. The most notable aspect of these contour plots is the fact that right under the indenter, strain gradient plasticity predicts a region of very low ϵ^p. Suppression of plasticity at notch tips have also been observed in similar simulations by Mikkelsen and Goutianos (2009). Secondly, the plastic zones produced by strain gradient plasticity are somewhat larger than those for conventional plasticity. The shapes are less circular at small depths though at higher depths, the shapes for the two cases become almost identical.

Suppression of plasticity right beneath the indenter is explained further through the contours of an effective measure of strain gradient (or GND density) $\|\nabla\epsilon^p\| = [(\epsilon^p_{,1})^2 + (\epsilon^p_{,2})^2]^{1/2}$ (see, Fig. 5(a)). Along X_1/l_*, the effective gradient attains a peak at $5l_*$ and again at $20l_*$. Also, values of the effective gradient at $X_1/l_* = 0$ are low. Assuming that the effective strain gradient is an indirect measure of the density of GNDs, this indicates that GNDs accumulate some

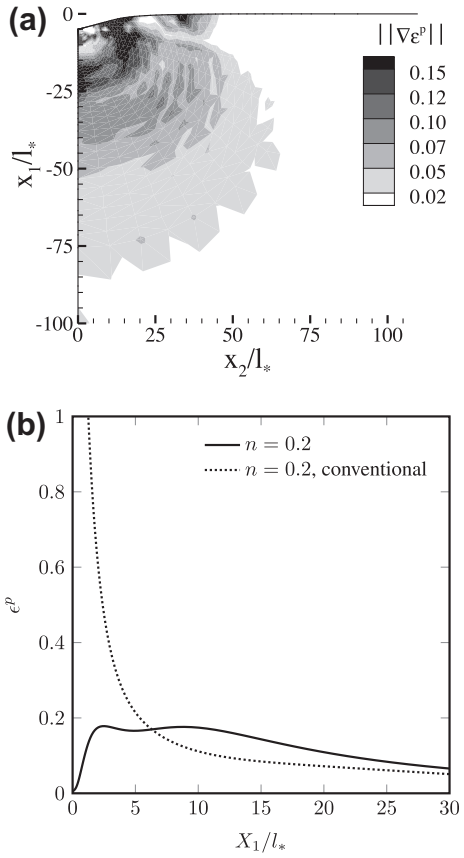

Fig. 5. (a) Contours of effective plastic strain gradient $\|\nabla\epsilon_p\|$ and (b) variation of ϵ_p with X_1/l_* for the cases with $n = 0.2$ and $\epsilon_0 = 0.001$ at $h/l_* = 5$.

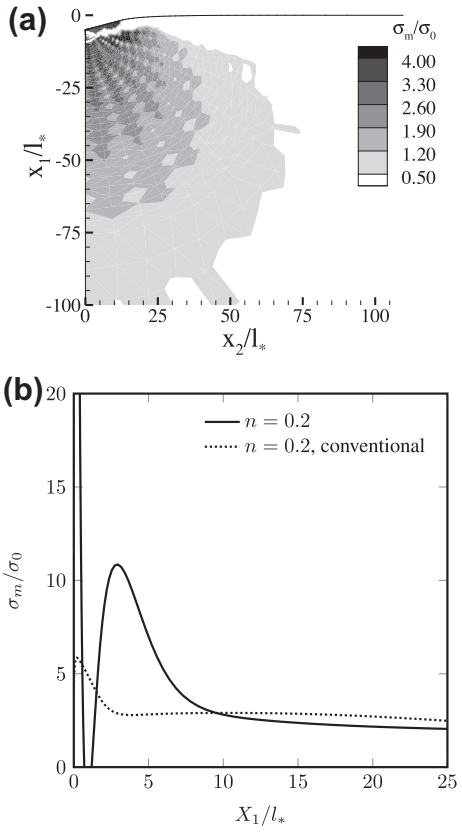

Fig. 6. (a) Contours of σ_m/σ_0 and (b) variation of σ_m/σ_0 with X_1/l_* for a material with $n = 0.2$ and $\epsilon_0 = 0.001$ at $h/l_* = 5$.

distance below the indenter tip according to the present model. Notably, significant GND accumulation occurs close to the free boundary $X_1 = 0$, outside the region of indentation, as well. The variation of plastic strain ϵ^p with X_1/l_* along with those derived with conventional plasticity have been shown in Fig. 5(b). In the conventional case, high gradients of plastic strain are seen in the region close to the indenter. On the contrary, in the case with strain gradient plasticity, this region experiences low plastic strains as the material tends to smoothen out the sharp gradients by hardening. Evidently, the distribution of ϵ^p and effective strain gradient $\|\nabla\epsilon^p\|$ shown in Fig. 4(c) and (d) and Fig. 5(a) are a result of the redistribution of the sharp gradients present in the conventional plasticity based simulations.

The effect of the smoothing out of the sharp gradients and the consequent hardening that results manifests in the contour plots of the mean stress σ_m/σ_0, shown in Fig. 6(a) and the variation of σ_m/σ_0 with X_1/l_* in Fig. 6(b). The mean stresses under the indenter, for both $n = 0.2$ and 0.5 are very high in case of gradient plasticity. The hardening effect of the high gradients beneath the indenter results in an increased load on it and leads to the ISE.

A discussion on the distribution of ϵ^p and the effective plastic strain gradient is in place here. Nix and Gao's (Nix and Gao, 1998) model assumes the existence of a circular volume of size a beneath the indenter where the GND density is constant. Finite Element analyses by Huang et al. (2006) based on a modified version of the Nix and Gao (1998) theory of strain gradient plasticity offers a more realistic picture. In their simulations, the GND density varies from a very high value under the indenter to zero over a roughly hemispherical region of size scale a. However, in our simulations, the region where gradient plasticity is active spreads over a much larger region. Moreover, the region right under the indenter tip has plasticity either suppressed or completely absent. Dislocation dynamics simulations by Balint et al. (2006) on single crystals with three slip planes do show a region of dislocation activity much larger in size than a. However, local lattice misorientations predicted by dislocation dynamics (Balint et al., 2006), crystal plasticity (Bouvier and Needleman, 2006) or experiments (Rester et al., 2007) on single crystals are different from the distribution of $\|\nabla\epsilon^p\|$ shown in Fig. 5(a). Recent experiments also seem to suggest that, unlike in simulations with strain gradient plasticity, the GND structure does not evolve in a self-similar manner even for the wedge indentation.

The thickness L of the block of material analysed here is large enough to preclude effects of the boundary conditions on the lower ($X_1 = L$) or side boundaries ($X_2 = \pm W$). Higher order gradient theories however, allow for the imposition of boundary conditions that may have significant effects on the hardness for smaller values of L. In our case, $u_i = \epsilon^p = 0$ is imposed on $X_1 = L$. While this does not have any effect when L is large (we use $L = 250l_*$) where we effectively simulate a block of infinite thickness, the boundary condition models a film of thickness L on a rigid substrate with an interface that is impermeable to dislocations. In Fig. 7(a) and (b) we show the distributions of ϵ^p at depths of $h/l_* = 1$ and 5 for a case where $L = 50l_*$. The distribution of the effective gradient of plastic strain at these depths is shown in Fig. 7(c) while a comparison between the hardness H/H_0 for the case with finite thickness and that depicted in Fig. 3(b) is shown in Fig. 7(d).

At $h/l_* = 1$, the distribution of plastic strain is exactly similar to that for an infinite block as shown in Fig. 4(a). At $h/l_* = 5$, the plastic zone spans the whole of the thickness and the effect of the boundary condition on the lower boundary is manifested in the hardness. The hardness (Fig. 7(d)) shows the initial ISE, attains a plateau identical to the case of the infinite block (note that H_0 is

same for the infinite and finite H cases reported here) but starts to rise again at around $h/l_* \simeq 5$. High plastic strain gradients (see, Fig. 7(c)) exist at a small distance away from the indenter tip and along the free surface, like for the $L \to \infty$ case. But, the gradients start to rise sharply close to the impermeable lower boundary indicating pile-up of dislocations there.

Saha and Nix (2002) have performed a range of experiments on soft metallic films on rigid substrates. After effectively removing experimental artifacts resulting from the changes in the reduced modulus with indentation depth, they concluded that strain gradient effects contribute to increase in hardness at depths below $0.3L$ and above $0.75L$. However, interestingly, the minimum of the H versus h plot is an indication of the true hardness of the material.

These observations are borne out by our results. The H/H_0 for the case with finite L decays down to the values predicted by the case with $L \to \infty$ before it rises again. As shown in Fig. 7(d), the fact that effects of the lower boundary are felt at depths as small as $0.1L$ is also seen from dislocation dynamics results of Balint et al. (2006) for the thinnest film simulated in their work. Recent dislocation dynamics simulations of cylindrical indentation of thin films on rigid substrates by Ouyang et al. (2010) (where a very simple slip system was used) show that for thin enough films, a region of width somewhat larger than $2a$ and height L has concentrates dislocations. This is again similar to the ϵ^p contours shown in Fig. 7(a) which pertains to a polycrystalline material.

It should be noted that in the simulations of Balint et al. (2006) the minimum in the hardness versus depth results for the thinnest films (thickness ~ 2 μm) did not reach H_0 unlike in the experiments of Saha and Nix (2002) and the present work. It is reasonable to expect that for L/l_* much smaller than what is assumed here, the minimum in the H versus h plot may not correspond to the true hardness of the material.

3.2.2. Effect of yield stress and hardening exponent on indentation

Fig. 8(a) shows the variation of equivalent plastic strain ϵ^p with X_1/l_* for the three materials analyzed in this work. The corresponding results from simulations with conventional plasticity have also been plotted. The variation of $\|\nabla\epsilon^p\|$ for the three cases with X_1/l_* are shown in Fig. 8(b).

Simulations with conventional plasticity invariably exhibit sharp variation in ϵ^p with X_1/l_* close to the indenter tip. For the low yielding material with low hardening ($\epsilon_0 = 0.001,\ n = 0.2$), the variation in ϵ^p with X_1/l_* is the slowest. It is the sharpest for the high yielding case ($\epsilon_0 = 0.01$).

As discussed earlier, strain gradient plasticity redistributes the sharp variations in ϵ^p that may occur in conventional plasticity. The outcome of the redistribution is shown through the redistributed variations of ϵ^p and $\|\nabla\epsilon^p\|$ with X_1/l_* in Fig. 8(a) and (b) respectively. For high yielding materials, a zone of almost no ϵ^p develops below the indenter. Equivalent plastic strain under the indenter is suppressed and smaller in the low yielding cases. Complete absence or suppression of plasticity leads to different levels of hardening below the indenter. In particular, a high yielding material experiences more suppression of ϵ^p and larger mean stresses and therefore exhibits higher hardness.

The effect of the hardening exponent n is less pronounced, but still significant. Though the levels of ϵ^p are similar to a low hardening material, the corresponding levels of $\|\nabla\epsilon^p\|$ are lower (see Fig. 8(b)). Consequently, higher levels of hardening due to gradient effects result also for high hardening materials. This leads to a moderate increases in hardness with n.

Redistribution of ϵ^p in the conventional case results in a new distribution of ϵ^p and $\|\nabla\epsilon^p\|$ in the cases with strain gradients. Low hardneing materials exhibit a 'two-humped' distribution of

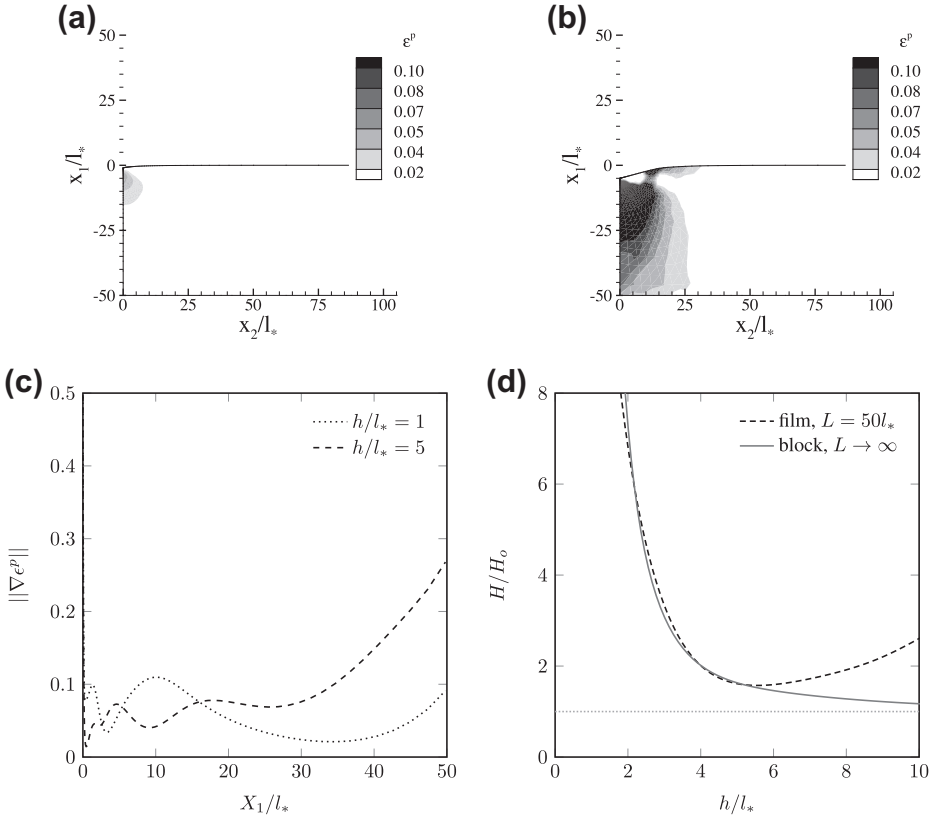

Fig. 7. Contour of equivalent plastic strain ϵ^p, at $h/l_* =$ (a) 1 and (b) 5 for a film of finite thickness $L = 50l_*$. (c) The variation of $\|\nabla\epsilon^p\|$ with X_1/l_*. (d) Comparison of hardness H/H_0 between the cases with $L = 50l_*$ and $L \to \infty$. For all cases $n = 0.2$ and $\epsilon_0 = 0.001$.

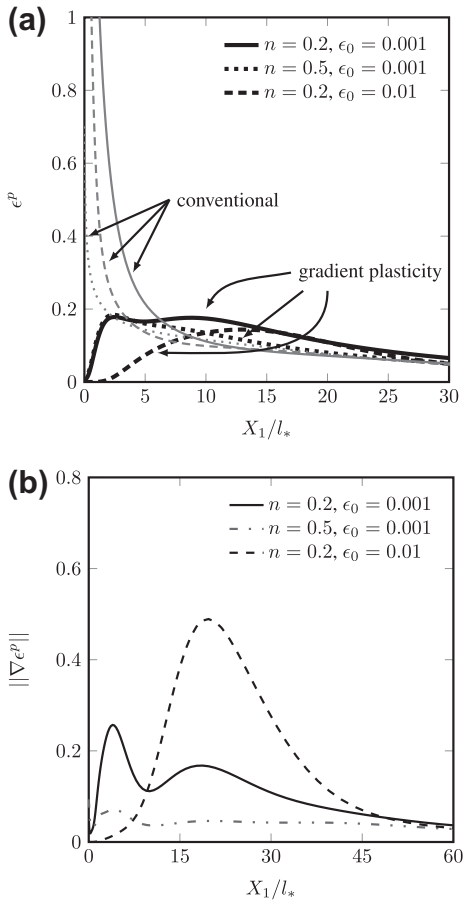

Fig. 8. (a) Variation of ϵ^p with X_1/l_* and (b) variation of $\|\nabla\epsilon^p\|$ with X_1/l_* for the cases analyzed, i.e. $\epsilon_0 = 0.001$, $n = 0.2$ and 0.5 and $\epsilon_0 = 0.01$ and $n = 0.2$. The variations for the corresponding conventional cases are also shown.

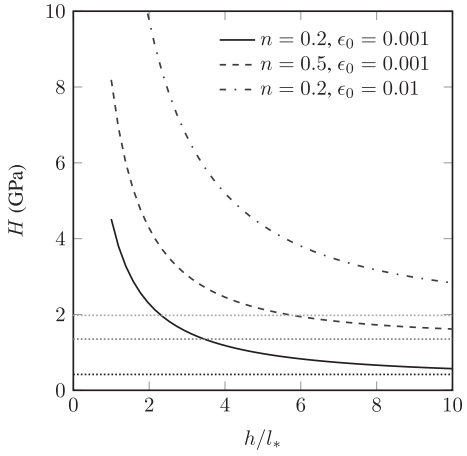

Fig. 9. Variation of H with h/l_* for the three different materials analyzed. The horizontal lines show the corresponding conventional hardness for these materials.

$\|\nabla\epsilon^p\|$ with X_1/l_*. Large gradients accumulates slightly below the indenter tip and at $X_1 \simeq 20l_*$.

Right under the indenter the gradients of ϵ^p are much lower for the high yielding material. Moreover, the gradient are maximum at $X_1 \simeq 20l_*$, with the region below the indenter exhibiting complete absence of $\|\nabla\epsilon^p\|$. This implies that a high total dislocation density

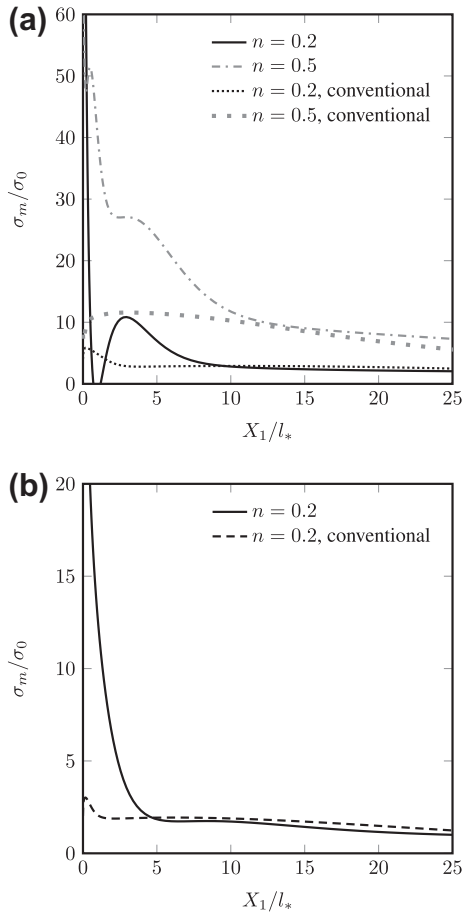

Fig. 10. Variation of mean stress σ_m with X_1/l_* for the cases analyzed, i.e. (a) $\epsilon_0 = 0.001$, $n = 0.2$ and $n = 0.5$ and (b) $\epsilon_0 = 0.01$ and $n = 0.2$. The variations for the corresponding conventional cases are also shown.

develops during indentation some distance away from the indenter tip rather than under it.

At this stage, it is possible to make some qualitative connections with experimental results. First compare the cases with $n = 0.2$ but different yield strains ϵ_0. Fig. 9 shows the hardness H versus h/l_* plots for all the three materials considered. The three horizontal lines in this figure indicate the hardnesses obtained from conventional plasticity. Clearly, the hardness increases with ϵ_0. Moreover, for $n = 0.2$, h^*/l_* for the case with higher yield stress is slightly higher than that for the low yielding case. In fact, from the fits using Eq. (62), we obtain $h^*/l_* \simeq 9$ for $\epsilon_0 = 0.01$ and $h^*/l_* \simeq 8$ for $\epsilon_0 = 0.001$. These approximately denote the values of h^*/l_* below which ISE becomes noticable.

However, though h^*/l_* seems to be relatively insensitive to ϵ_0, it should be noted that l_* for the two materials ($n = 0.2$ and $\epsilon_0 = 0.001$ and 0.01) need not be equal. In fact, Evans and Hutchinson (2009) have plotted the values of l_* for a number of materials obtained from comparisons with bending experiments. Their data (Fig. 13 of their paper) shows that l_* scales as $\epsilon_0^{-1.2}$. This implies that when the ratio of yield strains of two materials is 10, the ratio $h^*_{\text{high-yielding}}/h^*_{\text{low-yielding}} = 0.07$. In other words, when $(H/H_0)^2$ of these two materials is plotted against $1/h^2$ (or $1/h$), the slope is much *lower* for a material with *high yield stress*.

Qualitatively, this conclusion is supported by experiments though quantitative confirmation is difficult. Hardness data for iridium and MgO—yield strain of the latter being 50 times that of the former—has been plotted together by Huang et al. (2006). Iridium indeed has a much higher value of h^* than MgO.

A general conclusion that can be drawn from the above discussions is that low yielding materials have lower hardness and exhibit ISE at larger depths than high yielding materials. This conclusion is also supported by Fig. 10 where the variation of the mean stress σ_m/σ_0 has been plotted against X_1/l_*. In general, a low yielding, low hardening material needs to redistribute the high strain gradients seen in conventional plasticity over the longest distance. This is roughly indicated by the distance over which σ_m/σ_0 is larger than that computed from conventional plasticity. As seen from Fig. 10, this distance is about $10l_*$ at $h/l_* = 5$. However, for the materials with higher yield stress (see Fig. 10(b)), this distance, at the same value of h/l_*, is about $5l_*$. At any depth of indentation, the effects of strain gradient plasticity penetrate deeper into a low yielding material. This is also the reason for h^* being larger for these materials compared to high yielding ones.

Moreover, from the results of our simulations, irrespective of whether Eq. (3) or Eq. (62) is used, the fitting parameter h^*/l_* decreases with n. Thus, the present simulations also indicate that, yield stresses being equal, h^*/l_* for a high hardening material is smaller than a low hardening one. While this inference is difficult to verify experimentally, $\log(h^*/b)$ seems to *increase* linearly with n (where b is the Burger's vector) for a range of materials studied by Kim et al. (2008). This result does not necessarily contradict ours since for the various materials studied by them, both ϵ_0 and l_* are different.

3.2.3. Comparison between wedge and cylindrical indentation

As mentioned earlier, experimental hardness obtained from spherical indentation is known to be relatively insensitive to the depth of indentation (or radius of the contact area a) but depend on the size of the sphere. Here, we compare cylindrical and wedge indentations to show that the present model successfully brings out this effect.

To this end, we have used indenter radii R/l_* of 5–50 and the calculated hardness values H/σ_0 against a/R have been plotted in Fig. 11(a). For the smallest cylinder modeled, the hardness is the maximum and reduces to the values predicted by conventional plasticity as R increases. The hardness increases with a/R for small depths but quickly attains an almost constant, depth insensitive value. For a sufficiently large cylinder, the dependence on a/R is indeed negligible. This is in contrast to wedge indentation as shown in Fig. 11(b), where we have plotted the variation in H/σ_0 with a/l_* for the case with $n = 0.2$ and $\epsilon_0 = 0.001$. At contact width $a < 5l_*$, the wedge exhibits severe ISE unlike the cylinder with $R = 50l_*$.

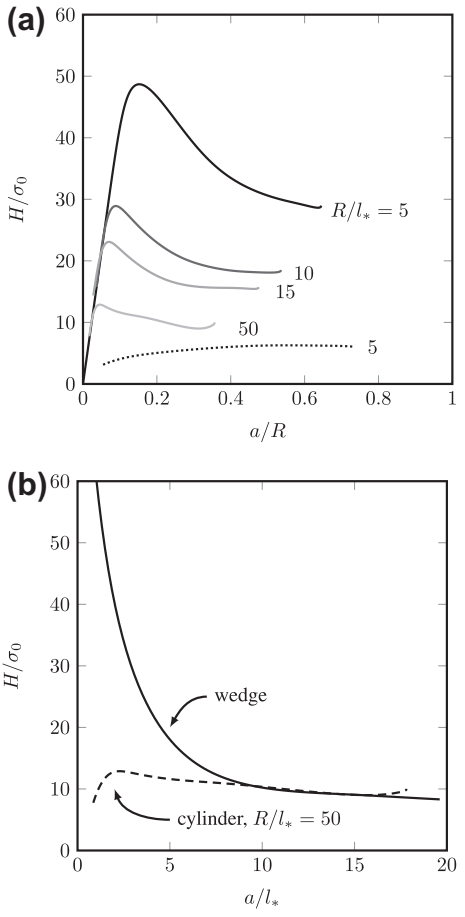

Fig. 11. (a) Variation of H/σ_0 with a/R for indentation with cylindrical punch and (b) comparison of H/σ_0 with a/l_* between indentations by wedge and cylindrical punch.

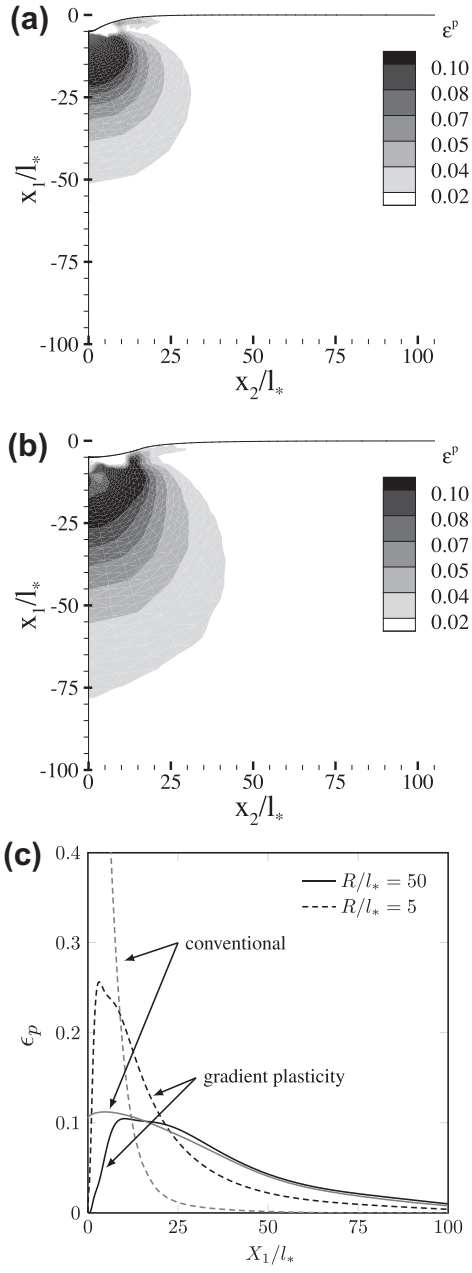

Fig. 12. Contour plots of ϵ^p under the cylindrical indenter for (a) $R/l_* = 5$ and (b) $R/l_* = 50$. (c) Variation of ϵ^p with X_1/l_* under the cylindrical punch. For all the cases $n = 0.2$, $\epsilon_0 = 0.001$ and $h = 5l_*$.

Beyond $a = 5l_*$, both the wedge and the cylinder give identical hardnesses.

Contours of the plastic strain ϵ_p for the cases with $R/l_* = 5$ and 50 have been shown in Fig. 12(a) and (b). For both these cases, properties for Material #1 have been used and $h = 5l_*$. Comparing Fig. 12(a) with Fig. 4(b) shows that $R = 5l_*$ yields plastic strains that are almost identical to that in a wedge indentation, at a similar depth h. On the other hand, for $R = 50l_*$, the suppression of plasticity below the indenter is much weaker. In fact, these plastic strain contours are quite like in the conventional case shown in Fig. 4(d).

The variation of ϵ^p with X_1/l_* for the case of cylindrical indentation (as shown in Fig. 12(c)) sheds more light on the dependence on R/l_*. According to conventional plasticity, the gradients of strain close to $X_1/l_* = 0$ are much stronger in case of $R/l_* = 5$ than for 50. Smoothing of the high gradient in strain gradient plasticity calls for a more drastic redistribution of ϵ^p and the effective strain gradient for $R/l_* = 5$. The variation of ϵ^p decays to the levels predicted by conventional plasticity at $X_1 \simeq 75l_*$. On the contrary, the case with $R/l_* = 50$ has a much gentler variation of ϵ^p to start with and drastic readjustments are not required when strain gradient plasticity is used. Consequently the variation of ϵ^p matches with the conventional case at $X_1 \simeq 10l_*$.

4. Conclusions

A Finite Element implementation of a strain gradient plasticity model (Fleck and Hutchinson, 2001) within the framework of large strain elasto-viscoplasticity has been used to study the indentation size effect for wedge and cylindrical indentation. The primary motivation for this study was to see whether results from strain gradient based simulations are, at least qualitatively, commensurate with experimental observations on shallow indentation.

Strain gradient plasticity models simulate the indentation size effect. The effect arises from the fact that the high strain gradients under the indenter predicted by conventional plasticity are redistributed over a region under the indenter into a smoother distribution of ϵ^p and $\|\nabla\epsilon^p\|$, in strain gradient plasticity. This leads to much higher stresses beneath the indenter than what is expected from conventional plasticity. The effect is especially pronounced at low depths of indentation.

The model used in this work predicts that ISE manifests at relatively higher depths of indentation in case of low yielding materials. This fact is borne out by experiments. However, the simulations also predict that yield stresses being equal, a high hardening material manifests ISE at lower depths of indentation. This is difficult to ascertain experimentally. The relative contributions of yield stress and hardening exponent in causing ISE remains to be explored further.

The shape and size of the plastic zone beneath the indenter and the distribution of strain gradients (which is an indicator of the distribution of GND) obtained from the simulations are intriguing. They indicate that density of dislocations are the highest at some depth away from the indenter tip rather than right under it. Also, the plastic zone is significantly larger than the contact width. While the latter inference is supported by some simulations using other techniques, most simulations and experiments show highest dislocation densities right under the indenter. In our simulations, plasticity is suppressed or sometimes, completely absent in the region right under the tip of the indenter. Note that the indented surface is assumed to be permeable to dislocations.

Experimentally, hardness derived from spherical indentation is known to be relatively depth independent but dependent on the size of the indenting sphere. By simulating cylindrical indentation and comparing it with the self-similar wedge, we have shown that the depth independence and size dependence of the former is correctly borne out. Also, the simulations were able to show an initial decrease and subsequent increase in hardness with depth of indentation for films bonded to a rigid substrate.

It should be mentioned that the present simulations pertain to micro-indentation as nano-indentation does not seem to follow the scaling with depth indicated by Eq. (3) (see Huang et al., 2006; Elmustafa and Stone, 2003; Lim and Chaudhri, 1999). Finite Element simulations using higher order strain gradient plasticity theories qualitatively capture most important experimental observations on micro-indentation even with a single, plastic strain independent length scale parameter l_*. A proper calibration of l_* and its physical interpretation remain issues that need to be addressed in the future.

Acknowledgments

Authors gratefully acknowledge the financial support from Department of Science and Technology (DST), Ministry of Science and Technology, Govt. of India for the present study.

References

Aifantis, E.C., 1984. On the microstructural origin of certain inelastic models. J. Eng. Mater. 106, 326–330.
Balint, D.S., Deshpande, V.S., Needleman, A., der Giessen, E.V., 2006. Discrete dislocation plasticity analysis of the wedge indentation of films. J. Mech. Phys. Solids 54, 2281–2303.
Begley, M.R., Hutchinson, J.W., 1998. The mechanics of size-dependent indentation. J. Mech. Phys. Solids 46, 2049–2068.
Bhattacharya, A.K., Nix, W.D., 1988a. Analysis of elastic and plastic deformation associated with indentation testing of thin films on substrates. Int. J. Solids Struct. 24, 1287–1298.
Bhattacharya, A.K., Nix, W.D., 1988b. Finite element simulation of indentation experiments. Int. J. Solids Struct. 24, 881–891.
Bhattacharya, A.K., Nix, W.D., 1991. Finite element analysis of cone indentation. Int. J. Solids Struct. 27, 1047–1058.
Borg, U., Niordson, C.F., Fleck, N.A., Tvergaard, V., 2006. A viscoplastic strain gradient analysis of materials with voids or inclusions. Int. J. Solids Struct. 43, 4906–4916.
Borst, R.D., Pamin, J., 1996. Some novel developments in finite element procedures for gradient-dependent plasticity. Int. J. Numer. Methods Eng. 39, 2477–2505.
Bouvier, S., Needleman, A., 2006. Effect of the number and orientation of active slip systems on plane strain single crystal indentation. Model. Simul. Mater. Sci. 14, 1105.
Durst, K., Backes, B., Göken, M., 2005. Indentation size effect in metallic materials: correcting for the size of the plastic zone. Scripta Mater. 52, 1093–1097.
Elmustafa, A.A., Stone, D.S., 2003. Nanoindentation and indentation size effect: kinetics of deformation and strain gradient plasticity. J. Mech. Phys. Solids 51, 357–381.
Evans, A.G., Hutchinson, J.W., 2009. A critical assessment of theories of strain gradient plasticity. Acta Mater. 57, 1675–1688.
Feng, G., Nix, W.D., 2004. Indentation size effect in MgO. Scripta Mater. 51, 599–603.
Fleck, N.A., Hutchinson, J.W., 1997. Strain gradient plasticity. Adv. Appl. Mech. 33, 295–361.
Fleck, N.A., Hutchinson, J.W., 2001. A reformulation of strain gradient plasticity. J. Mech. Phys. Solids 49, 2245–2271.
Fleck, N.A., Muller, G.M., Ashby, M.F., Hutchinson, J.W., 1994. Strain gradient plasticity: theory and experiment. Acta Metall. Mater. 42, 475–487.
Freund, L.B., Suresh, S., 2003. Thin Film Materials Stress, Defect Formation and Surface Evolution. Cambridge University Press, Cambridge.
Huang, Y., Zhang, F., Hwang, K.C., Nix, W.D., Pharr, G.M., Feng, G., 2006. A model of size effects in nano-indentation. J. Mech. Phys. Solids 54, 1668–1686.
Johnson, K.L., 1970. The correlation of indentation experiments. J. Mech. Phys. Solids 18, 115–126.
Kim, J.-Y., Kanga, S.-K., Lee, J.-J., il Jang, J., Lee, Y.-H., Kwon, D., 2007. Influence of surface-roughness on indentation size effect. Acta Mater. 55, 3555–3562.
Kim, J.-Y., Kang, S.-K., Greer, J.R., Kwon, D., 2008. Evaluating plastic flow properties by characterizing indentation size effect using a sharp indenter. Acta Mater. 56, 3338–3343.
Lim, Y.Y., Chaudhri, M.M., 1999. The effect of indenter load on the nanohardness of ductile metals: an experimental study on polycrystalline work-hardened and annealed oxygen-free copper. Philos. Mag. A 79, 2979–3000.
Liu, Y., Ngan, A.H.W., 2001. Depth dependence of hardness in copper single crystals measured by nanoindentation. Scripta Mater. 44, 237–241.
Ma, Q., Clarke, D.R., 1995. Size dependent hardness of silver single crystals. J. Mater. Res. 10, 853–863.
McElhaney, K.W., Vlassak, J.J., Nix, W.D., 1998. Determination of indenter tip geometry and indentation contact area for depth-sensing indentation experiments. J. Mater. Res. 13, 1300–1306.
Mikkelsen, L.P., Goutianos, S., 2009. Suppressed plastic deformation at blunt crack-tips due to strain gradient effects. Int. J. Solids Struct. 46, 4430–4436.

Niordson, C.F., Redanz, P., 2004. Size-effects in plane strain sheet-necking. J. Mech. Phys. Solids 52, 2431–2454.
Nix, W.D., Gao, H., 1998. Indentation size effects in crystalline materials: a law for strain gradient plasticity. J. Mech. Phys. Solids 46, 411–425.
Oliver, W., Pharr, G., 2004. Measurement of hardness and elastic modulus by instrumented indentation: advances in understanding and refinements to methodology. J. Mater. Res. 19, 3–20.
Ouyang, C., Li, Z., Huang, M., Fan, H., 2010. Cylindrical nano-indentation on metal film/elastic substrate system with discrete dislocation plasticity analysis: a simple model for nano-indentation size effect. Int. J. Solids Struct. 47, 3103–3114.
Pharr, G.M., Herbert, E.G., Gao, Y., 2010. The indentation size effect: a critical examination of experimental observations and mechanistic interpretations. Annu. Rev. Mater. Res. 40, 271–292.
Poole, W.J., Ashby, M.F., Fleck, N.A., 1996. Micro-hardness of annealed and work-hardened copper polycrystals. Scripta Mater. 34, 559–564.
Qiao, X.G., Starink, M.J., Gao, N., 2010. The influence of indenter tip rounding on the indentation size effect. Acta Mater. 58, 3690–3700.
Rester, M., Motz, C., Pippan, R., 2007. Microstructural investigation of the volume beneath nanoindentations in copper. Acta Mater. 55, 6427–6435.
Saha, R., Nix, W.D., 2002. Effects of the substrate on the determination of thin film mechanical properties by nanoindentation. Acta Mater. 50, 23–38.
Shi, M.X., Huang, Y., Gao, H., 2004. The J-integral and geometrically necessary dislocations in nonuniform plastic deformation. Int. J. Plast. 20, 1739–1762.
Stölken, J.S., Evans, A.G., 1998. A microbend test method for measuring the plasticity length scale. Acta Mater. 46, 5109–5115.
Swadener, J.G., George, E.P., Pharr, G.M., 2002. The correlation of the indentation size effects measured with indenters of various shapes. J. Mech. Phys. Solids 50, 681–694.
Tabor, D., 1951. The Hardness of Metals. Clarendon Press, Oxford.
Wei, Y., Hutchinson, J.W., 2003. Hardness trends in micron scale indentation. J. Mech. Phys. Solids 51, 2037–2056.